RSC Advances

ROYAL SOCIETY OF CHEMISTRY

www.rsc.org/advances

1-ethyl-2,3-dimethylimidazolium paramagnetic ionic liquids with 3D magnetic ordering in its solid state: synthesis, structure and magneto-structural correlations

Abel García-Saiz[a], Imanol de Pedro[a]*, Oriol Vallcorba[b], Pedro Migowski[c], Ignacio Hernández [a,d], Luis Fernandez Barquin[a], Isaac Abrahams[e], Majid Motevalli[e], Jairton Dupont[c], Jesús Antonio Gonzalez[a] and Jesús Rodríguez Fernández[a]

[a] CITIMAC, Facultad de Ciencias, Universidad de Cantabria, Santander 39005, Spain.
[b] ALBA Synchrotron Light Source, Cerdanyola del Vallés, Barcelona, Spain.
[c] Universidade Federal do Rio Grande do Sul, Porto Alegre, Brazil.
[d] Materials Research Institute, School of Physics and Astronomy, Queen Mary University of London, London E1 4NS, United Kingdom.
[e] Materials Research Institute, Department of Chemistry and Biochemistry, School of Biological and Chemical Sciences, Queen Mary University of London, London E1 4NS, United Kingdom.
E-mail: depedrovm@unican.es

Abstract

Two novel paramagnetic ionic liquids, comprised of 1-ethyl-2,3-dimethylimidazolium (Edimim) cation and tetrahaloferrate(III) (FeX_4) (X = Cl and Br) anion were synthetized and characterized by thermal, structural, Raman spectroscopy and magnetic studies. The crystal structures, determined by synchrotron X-ray powder diffraction and single crystal X-Ray diffraction at 100 K for Edimim[$FeCl_4$] and Edimim[$FeBr_4$] respectively, are characterized by layers of cations (in non-planar configuration) and anions stacked upon one another in a three-dimensional (3D) manner with several non-covalent interactions: halide-halide, hydrogen bond and anion-π. Magnetization measurements show the presence of three-dimensional antiferromagnetic ordering below Neel temperature (T_N) with the existence of a noticeable magneto-crystalline anisotropy in the bromide compound. The corresponding magneto-structural correlations evidence that the 3D magnetic ordering mainly takes place via Fe-X---X-Fe (X = Cl and Br) interactions, displaying a higher superexchange magnetic interaction between the planes. Comparison with the Emim[FeX_4] (X = Cl and Br) phases (Emim: 1-ethyl-3-methylimidazolium) reveals that the methylation at C(2) position onto imidazolium cation ring causes an increase of the melting point and a decrease of the T_N. In contrast, the comparative study with Dimim[FeX_4] (X = Cl and Br) compounds (Dimim: 1,3-dimethylimidazolium) shows a lower T_N in the chloride compound, Edimim[$FeCl_4$], whereas it is higher for the bromide, Edimim[$FeBr_4$]. This fact is attributed to the spin delocalization of iron atoms in $[FeBr_4]^-$ and discards the hypothesis that a bigger imidazolium ion size causes a weaker magnetic coupling in paramagnetic ionic liquids based on tetrahaloferrate anion and imidazolium cation with 3D magnetic ordering in its solid state.

Keywords: paramagnetic Ionic Liquids; Crystal Structure; Three-Dimensional Magnetic Ordering; non-covalent Interactions; Magneto-structural correlations.

Introduction

Paramagnetic ionic liquids are molten salts formed entirely of ions which have a melting point below 100 ºC.[1] They have received considerable attention among ionic liquids (ILs),[2] fuelled by the possibility of tuning the materials properties by means of external magnetic fields[3] or using them in the liquid state to produce nanoparticle-free magnetic emulsions and microemulsions.[4] Moreover, they can combine magnetic[5] and ILs properties with additional intrinsic thermochromic,[6] magneto-electrochromic[7] or luminescent[8] properties depending on the enclosed paramagnetic ion used. Thus, reports on the synthesis, study and application of these smart materials has proliferated. The first compounds developed since their discovery by the group of Hayashi,[9] contained a metal anion (such as iron,[10, 11] copper,[12] manganese[13]) and an organic cation, typically imidazolium, pyrrolidinium, pyridinium[14] or tetraalkylphosphonium.[15] Currently, the combinations of different rare-earth (europium,[16] neodymium,[17] dysprosium,[5] etc.) chiral amionacids,[18] dicationic ions[19] tricationic ions[20] or heteroanions[21], etc. have been studied for applications transport and separation of materials[22], separation of greenhouse gases (CO_2) through supported magnetic ionic liquids membranes,[23] magnetic surfactants[24], extraction of DNA[25] or esterification of oleic acid to biodiesel.[26]

ILs based on imidazolium cation have also recently received attention for the experimental[27, 28] and theoretical[29] study of non-covalent interactions and cohesion properties.[30, 31] Convincing results indicate that the structural organization in the solid state can be extensible to the liquid phase and is apparently maintained to the gas phase[32, 33]. Many groups have focused their studies on the dipole-dipole, and hydrogen bonds within the crystal and molecular structures of these ILs[34] in order to improve the understanding of these forces, aim at a fine tailoring of their technological applications. Importantly, in ILs based on imidazolium cation with paramagnetic anions, such as the presented compounds, it is also necessary to investigate other non-bonding interactions, like halogen-halogen[35] (between the nearest metal complex anions) or anion-π[36] (between the anion and cation) as these interactions play an important role in the organization of their structural units. In addition, if these non-bonding contacts are strong, interesting collective electrical and magnetic phenomena can arise, such as ferroelectricity in the bis(imidazolium) pentachloroantimonate (III), $(C_3N_2H_5)_2SbCl_5$, or a three-dimensional (3D) magnetic ordering in ILs based on tetrahaloferrate ions.[37, 38] Moreover, changing the external conditions, such as pressure, shows an influence in the magnetic coupling, such as in Emim[$FeCl_4$], which vary from antiferromagnetic (AF) to ferrimagnetic ordering.[39]

The learning of magneto-structural correlations in ILs based on tetrahaloferrate anion and imidazolium cation need a comprehensive understanding through a systematic investigation of a wide variety of compounds by changing the cationic and anionic structures. To accomplish this objective, we set out to study the family of ILs based on the tetrahaloferrate ion and 1,3-dimethylimidazolium cation. Our results reveal that (i) halogen-halogen interactions are the main force inducing the 3D magnetic ordering in the solid state of this type of ILs[40] (ii) the spin population in the metal complex anion together with the distances and angles between the superexchange pathways [Fe-X---X-Fe (X = halide)] play a decisive role in attaining the 3D magnetic ordering [40] and (iii) a less electronegative halide ion rises the efficiency of the magnetic couplings.[41] Interestingly, it has also been shown that changes in the alkyl chain length of imidazolium cation cause variations in other physicochemical properties, including viscosity, density, conductivity, and melting point. [42 43]

Herein, we want to explore the effects on the thermal and magnetic properties of the methylation at C(2) position [N-C-N site] onto imidazolium cation, with different metal complex cations. We report on the synthesis, thermal, Raman and magnetic properties of two novel paramagnetic ionic liquids, namely 1-ethyl-2,3-dimethylimidazolium tetrachloroferrate, Edimim[$FeCl_4$], and 1-ethyl-2,3-dimethylimidazolium tetrabromoferrate, Edimim[$FeBr_4$], together with the single crystal structure data with regard to obtaining the magneto-structural relationship.

Experimental Section

Synthesis: All chemicals, anhydrous $FeCl_3$ (99.9 %, Aldrich), anhydrous $FeBr_3$ (98.5 %, Aldrich) 1,2-dimethylimidazole (98%, Sigma-Aldrich), acetonitrile (HPLC grade, Vetec), ethyl iodide (98%, Acros) were purchased from commercial sources and used without any further purification. All manipulations were made in air atmosphere, except otherwise stated in the text.

1-ethyl-2,3-dimethylimidazolium iodide: 1,2-dimethylimidazole (9.38 g, 97.5 mMol) was dissolved in 150 mL acetonitrile and ethyl iodide (11.68 g, 107.25 mmol) was added dropwise to the stirred solution cooled in an ice bath. After addition of the iodoethane, the reaction mixture was warmed up and the mixture refluxed for 24h. The reaction was cooled down and the solvent removed under vacuum. The remaining solids were re-crystallized in a mixture of acetone: acetonitrile yielding white crystals 15.80 g, 79% yield.

1-ethyl-2,3-dimethylimidazolium tetrachloroferrate: 1-ethyl-2,3-dimethylimidazolium iodide (5 g, 19.84 mMol) was dissolved in 500 mL of distilled water and passed through an anion exchange column Amberlite IRA-400 column (OH- form) to yield a iodide free solution of 1-ethyl-2,3-dimethylimidazolium hydroxide (test by the Volhard method). The hydroxide solution was neutralized with concentrated hydrochloric acid (36%, Vetec) topH 7 and water removed in rotary evaporator with the remaining water removed under vacuum at 100ºC. The solids were then dissolved in dichloromethane and dried over anhydrous Na_2CO_3, filtered and the solvent removed under vacuum, yielding 4.80 g (96%) of 1-ethyl-2,3-dimethylimidazolium chloride.

In a glove-box, the 1-ethyl-2,3-dimethylimidazolium chloride (1 g, 4.90 mmol) was mixed with anhydrous $FeCl_3$ (0.795 g, 4.90 mmol) in a 8 mL vial. The mixture was heated at 100ºC and the desired product was obtained as a red solid., 1.795 g (100% yield),

1-ethyl-2,3-dimethylimidazolium tetrabromoferrate: 1-ethyl-2,3-dimethylimidazolium bromide was prepared the same way as 1-ethyl-2,3-dimethylimidazolium chloride, except for the use of hydrobromic acid (47%, Vetec) instead of HCl, affording 4.70 g (94% yield).

In a glove-box , the 1-ethyl-2,3-dimethylimidazolium bromide (0.863 g, 4.23 mmol) was mixed with anhydrous $FeBr_3$ (1.25 g, 4.23 mmol) in a 8 mL vial. The mixture was heated at 100ºC and the desired product was obtained as a brown-reddish solid., 2.113 g (100% yield).

Chemical analysis: Microanalytical data (C, H and N) were obtained with an Elemental model Vario 51 MACRO elemental analyzer. Iron, chlorine and bromine contents were determined with a Spectra Spectrometer DCP-AEC after dissolving a weighed amount of sample in water (aq).Chemical formula $C_5N_2H_9Cl_4Fe$ and $C_5N_2H_9Br_4Fe$ are confirmed. *Thermal analysis*: A Mettler-Toledo (TGA/SDTA851 and DSC822) was used for the thermal analyses in an oxygen dynamic atmosphere (50 ml/min) at a heating rate of 10 °C/min. For this experiment, ca. 15 mg of powder sample was thermally treated, and blank runs were performed.

Elemental analysis for $C_7N_2H_{13}Cl_4Fe$ (Edimim[$FeCl_4$]). Calcd: C, 26.0; N, 8.67; H, 4.10; Cl, 43.93; Fe, 17.30 %; found C, 25.8; N, 8.63; H, 4.16; Cl, 44.17; Fe, 17.24 %. Elemental analysis for $C_7N_2H_{13}Br_4Fe$ (Edimim[$FeBr_4$]). Calcd: C, 16.79; N, 5.59; H, 2.63; Br, 63.84; Fe, 11.15 %; found: 16.70; N, 5.54; H, 2.59; Br, 64.08; Fe, 11.09

***Raman spectroscopy**:* The non-polarized Raman spectra were recorded in backscattering geometry with a Horiba T64000 triple spectrometer with a confocal microscope in subtractive mode that had a resolution of 0.6 cm^{-1}. A 1800 grooves/mm grating and a 100-µm slit were used with a liquid N2-cooled CCD detector (Jobin-Yvon Symphony). A 647 nm line of a Coherent Innova Spectrum 70C Ar^+-Kr^+ laser was focused down with a 20x objective and the power on the sample kept below 5 mW to avoid laser-heating effects on the material being tested and the concomitant softening of the observed Raman peaks.

Magnetic measurements: Temperature dependence of the magnetic susceptibility measurements were performed using a standard QD PPMS magnetometer by heating from 2 to 300 K at several magnetic fields, from 1 to 85 kOe, after cooling in either the presence (field cooling, FC) or the absence (zero field cooling, ZFC) of the applied field. Magnetization as a function of field (*H*) was measured using the same magnetometer in the $-85 \leq H/\mathrm{kOe} \leq 85$ range at 2 and 15 K after cooling the sample in zero field. Heat capacity has been measured using the same magnetometer between 2 and 300 K at several magnetic fields, from 0 to 85 kOe, with a standard relaxation method using a two-tau model. In order to guarantee a good thermal contact, apiezon N grease was used to glue the sample to the sample-holder. The addenda (sample-holder plus grease) was measured at different magnetic fields before the sample measurements and then subtracted from the total heat capacity in order to get the sample heat capacity. The sample was a 5 mg plate obtained compressing the original thin powder.

***Structural characterization**: **S**ynchrotron* **powder X-ray diffraction:** Data of Edimim[$FeCl_4$] at 100K were collected at the MSPD beamline (BL04) of ALBA Synchrotron using the microstrip MYTHEN-II detector (six modules, 1280 channels/module, 50 µm/channel, sample-to-detector distance 550mm) with an energy of 20KeV (refined wavelength of 0.6193 Å). The specimen was introduced into a 0.7 mm glass capillary and an Oxford cryostream 700 series was used to cool down the sample. The pattern was collected from 1.1 to 43º (2θ) with a total acquisition time of 60 seconds. The diffraction pattern was indexed using DICVOL04[44] and the intensities extracted with DAjust software[45] were introduced in the direct-space solution program TALP[46] to solve the crystal structure. The crystal structure was refined with the restrained Rietveld refinement program RIBOLS using distance restraints taken from Mogul.[47] Hydrogen atoms were placed in calculated positions and constrained to the corresponding C atoms in the final set of refinement cycles.

X Ray Single-Crystal Diffraction: Single crystals of Edimim[$FeBr_4$] were grown from the slow cooling of the microcrystalline powder in a vacuum sealed glass ampoule at 370 K in a 30 cm vertical Bridgman furnace ascending at a speed of 0.03 mm/min. The structure was determined by single crystal X-ray diffraction at 100 K. Data were collected using Mo Kα radiation (0.71073 Å) using a Bruker Apex 2 CCD diffractometer fitted with a Triumph monochromator. A single crystal of the compound, with approximate dimensions 0.06 mm × 0.06 mm × 0.10 mm was mounted on a glass fiber using silicon oil and cooled using a Cryostream cooler. Data were corrected for absorption using the multi-scan approach with the program SADABS[48], with minimum and maximum transmission coefficients of 0.3963 and 0.7457, respectively. Structure solution was carried out by Patterson methods using SHELXS-97 and the structure refined using SHELX-97[49]. Disorder in the imidazolium cation was modelled using two parts (refined part ratio of 0.56(1):0.44(1)), with atoms C1', C1'' and C2'' common to both parts. H-atoms were refined separately for both parts in their geometrical positions using an atom-riding model. Anisotropic thermal parameters were refined for all non-hydrogen atoms, with those within the disordered imidazolium ring restrained to be similar to neighboring atoms. The final anisotropic full-matrix least-squares refinement on F2 with 146 variables and 72 restraints converged at R1 = 6.18%, for the observed data and wR2 = 15.63% for all data. The goodness-of-fit was 1.053. The largest peak and hole in the final difference electron density synthesis were 1.306 and -1.174 electrons/$Å^3$, respectively, with an RMS deviation of 0.237 electrons/$Å^3$. On the basis of the final model, the calculated density was 2.333 g cm^{-3}, with F(000) = 470 electrons. Structure diagrams were generated within the Bruker Apex 2 suite of programs

Results and Discussion

Thermal investigations show that Edimim[$FeCl_4$] displays a solid-solid transition at 302 K and a melting point near 317 K. In Edimim[$FeBr_4$], there is a solid-solid transition at 301 K and the melting point is located at 352 K (see Fig. 1). The melting point (T_m) of the bromide compound is markedly higher than that of chloride sample, consistent with greater interionic interactions present in Edimim[$FeBr_4$]. A similar trend was observed for Emim [AlX_4][50] (T_m: 281 K for X = Cl and 323 K for X = Br) and Emim [FeX_4][51] (T_m: 291 K for X = Cl and 316 K for X = Br) ILs. Upon further heating, Edimim[$FeCl_4$] starts to decompose at a temperature of 548 K and Edimim[$FeBr_4$] at 571 K, offering a wide liquid region ≈ 200 K. (see inset of Fig. 1).

Fig. 1

The crystal structure of Edimim[$FeCl_4$] at 100 K was solved from synchrotron X-ray powder diffraction data using the direct-space method TALP[46] and refined with the restrained Rietveld refinement program RIBOLS using distance restraints taken from Mogul[47]. Hydrogen atoms were placed in calculated positions and constrained to the corresponding C atoms in the final set of refinement cycles. The experimental, calculated and difference powder profiles are displayed in Fig. S1. For Edimim[$FeBr_4$], the crystal structure was determined by single crystal X-Ray diffraction at 100 K. Atomic coordinates, interatomic distances and thermal parameters for both compounds are listed in the Supporting Information as well as the corresponding CIF files. Crystallographic data and structure refinement details are presented in Table 1. The most relevant intermolecular distances are displayed in Table 2 and 3.

Table 1

Table 2

Table 3

Fig. 2 illustrates the crystal structure of Edimim[$FeCl_4$] and Edimim[$FeBr_4$] at 100 K. Edimim[$FeCl_4$] crystallizes in the monoclinic crystal system, space group $P2_1/n$, with a=9.6703(1), b=14.3513(2), c=9.5744(1) Å and β = 94.261(1)º [V= 1325.08(3) $Å^3$, Z=4, ρ_{calcd}=1.618 gcm^{-3}]. The crystal structure of Edimim[$FeBr_4$] is also monoclinic, space group $P2_1$, a = 6.957 (6) Å, b = 14.804 (12) Å, c = 7.232 (6) Å and β = 90.728(14)º [Z=2, ρ_{calcd}=2.23 gcm^{-3}]. Both frameworks, projected along *b* direction, can be described as a stacking of $[Edimim]^+$ and $[FeX_4]^-$ (X =Cl and Br) intercalated layers changing orientation from layer to layer, with Fe···Fe distances larger than 6.5 Å inside the layer (Fig S2). For Edimim[$FeCl_4$] they also lie antiparallel to each other along the *c* axis, while they are stacked identically one above the other in the *a* direction. The topological description of the $[FeX_4]^–$ units (X = Cl and Br) of both compounds involves a tetrahedral geometry, with a mean X–Fe–X bond angle of 109.5(2) and 109(1)º and mean Fe–X bond distances of 2.21(1) and 2.36(1) Å for chloride and bromide derivatives, respectively. In the case of $[Edimim]^+$ units, the imidazole ring is aromatic and planar with all the refined values for the C–C and C–N bond lengths laying in the expected range of other imidazolium compounds.[41, 52] Furthermore, the conformational equilibria of the imidazolium cation has a gauche (non-planar) conformation with respect to NCC angle of the ethyl group, in good agreement with the conformation found in other ILs with 1-ethyl-3-methylimidazolium cation.[39, 53] The values of the C2-N1-C1'-C2' torsion angle for Edimim[$FeCl_4$] point to 85(1)º, whereas for Edimim[$FeBr_4$] the corresponding one is 83(3)º.

Fig. 2

Inspection of the crystallographic data of both compounds at 100 K and corresponding contrast with each specification rule, three types of non-covalent interactions are detected: (a) halide-halide, (b) hydrogen bonds and (c) anion-π. Four halide-halide interactions between the nearest $[FeCl_4]^–$ metal complex anions (Fig. 3a) arise in Edimim[$FeCl_4$]. Similarly, $[FeBr_4]^–$ has three probable contacts in the unit cell (Fig. 3b), in the case of Edimim[$FeBr_4$]. These non-covalent interactions propagate in a zigzag manner along the *b* axis [4.171(5) and 4.095(4) Å] and as linear chains across *ac* plane [distances between 3.936(5) and 4.192(4) Å and from 3.985(5) to 4.053(6) Å for Cl and Br, respectively]. These interactions must be taken into consideration even though they are longer than the sum of the vdw-radii (< 3.7 and 3.9 Å, respectively), since they are responsible for establishing of the 3D magnetic ordering (see the magnetic results below). The Fe···Fe distances are too long to consider direct magnetic interaction between metal atoms. They are in agreement with previous studies about the most frequent stacking distance of two metal complex anion in other paramagnetic ILs based on halometallates.[40, 54] Cation-anion interactions are characterized by an anisotropic H bonding network of twelve and nine hydrogen bonds between the halides and the surrounding $Edimim^+$ cations for Edimim[$FeCl_4$] and Edimim[$FeBr_4$], respectively (according to IUPAC rules for H bonds; Table 2 and 3 and Fig. 4). The shortest H-bond is between C5-H5•••Cl3 and C1´´-H´1B´´´•••Br4, with hydrogen contact distances of 2.751(10) and 2.72(1) Å, respectively. It is worth noting that the nearest imidazolium centroid···Cl$^-$ contact for Edimim[$FeCl_4$] [3.454(6) and θ = 100.43(16)º] is smaller than the most common value considered to indicate anion–π interaction (≤ 3.65 Å and θ = 90 ± 10º).[55] However, the corresponding distance for Edimim[$FeBr_4$] [4.003(10) and θ = 61.4(14)º] is larger than the specification rule. Nevertheless the Edimim[$FeBr_4$] compound displays two contacts above the ring periphery which are smaller than the sum of the vdw radii in Br···C and Br···[C-N] (≤ 3.75 and 3.70 Å respectively). These show interaction distances of 3.734(12) and 3.678(6) Å for Br3···C2 and Br3···[N3-C2] respectively [see Fig. 5 and Table 2 and 3], representative of weak anion–π interactions[56]

Fig. 3

Fig. 4

Fig. 5

Fig. 6 shows the non-polarized Raman spectrum of the Edimim[$FeCl_4$] sample between 50 and 3300 cm^{-1} at room temperature with excitation at 647 nm. These data offer the possibility of studying the conformational analysis of the Edimim$^+$ cation and the metal complex anion of this phase at room temperature (RT). The measured frequencies and their corresponding assignment in terms of the involved vibrational modes of the molecular ions are summarized in Table 4. We observe four Raman-active modes in the low-frequency region (see left-inset of Fig. 6, black) belonging to the symmetry point group T_d of the [$FeCl_4$]$^-$ iron complex. The peaks at ν_s = 110 and ν_{as} = 135 cm^{-1} are attributed to the bending modes and the other two, ν_s = 332 and ν_{as} = 338 cm^{-1}, respectively are related to the stretching modes of the Fe-Cl bond. In the same inset of Fig. 6 also shown are the four Raman-active vibration modes of the [$FeBr_4$]$^-$ iron complex of Edimim[$FeBr_4$] at RT (in red), with frequencies ν_s = 70 and ν_{as} = 90 cm^{-1} (bending modes) and ν_s = 201 and ν_{as} = 285 cm^{-1} (stretching). All these vibrational data agree with literature values for other compounds with tetrahaloferrate(III) anions[57, 58], corroborating that the presented compounds encompass the [FeX_4]$^-$ (X = Cl and Br) units, ruling the presence of [Fe_2X_7]$^-$ dimers.

Table 4

Fig. 6

The Raman bands observed between 390 and 3200 cm^{-1} (Fig. 6 and Table 4) of Edimim[$FeCl_4$] are assigned to the Edimim$^+$ cation. These bands may be compared with the theoretical and experimental vibrational frequencies of Emim$^+$ [39] and Dimim$^+$ cation; [40] which have been previously reported for other members of the imidazolium-based paramagnetic ILs. We attribute the Raman peak located at 394 cm^{-1} to the gauche non-planar geometry of the conformers [53, 59] given the conformational equilibrium of the Emim$^+$ cation across the CH_2−N bending mode of the ethyl chain [(trans−gauche) (planar−non-planar)]. This peak is also observed in the bromide compound at 303 cm^{-1}. The absence of a Raman signal between 430 and 450 cm^{-1} (where the vibrational frequencies of the trans planar geometry typically appear) rules out the presence of this conformer. The ring in-plane symmetric stretching and bending modes[60] (see Table 4) are found in the 500−1600 cm^{-1} range. Finally, the most intense peaks between 2700 and 3200 cm^{-1} (see right-inset of Fig. 6 and Table 4) correspond to the terminal CH_3, the ring CH_3 and the ethyl chains (symmetric and asymmetric H−C−H stretch) and the other, weaker ones (some of which overlap), to a ring N−C(H)−N (C−H stretch) modes, and a mixture of a ring HC=CH symmetric stretch and a ring in-plane symmetric stretch modes.[39, 60]

Variable temperature magnetic susceptibility measurements of the presented compounds were carried out on powdered samples in the 2−300 K temperature range. The temperature dependence of the molar magnetic, χ_m, and the reciprocal, χ_m^{-1}, susceptibilities measured under 1 kOe are represented in Fig. 7. The linear behavior of

χ_m^{-1} at temperatures higher than 20 K can be fitted to a Curie-Weiss law for both compounds. The calculated values give an effective paramagnetic moment (μ_{eff}) of 5.62 and 5.93 μ_B and paramagnetic Weiss temperatures (θ_P) of -1.0 and -12.5 K for Edimim[FeCl$_4$] and Edimim[FeBr$_4$], respectively. Both effective paramagnetic moments agree with the expected value for high spin d^5 Fe(III) ions (μ_{eff} = 5.92 μ_B per Fe ion) and the negative θ_P is a signature of an overall antiferromagnetic (AF) ordering when both compounds are frozen, in good agreement with those found in other paramagnetic ILs[40, 41] and paramagnetic salts[61] based on tetrahaloferrate ions. In addition, the results confirm that a less electronegative halide ion in the metal complex cation rises the efficiency of the magnetic couplings.[41]

Fig. 7

In the low temperatures regime, χ_m increases and reaches a maximum at 2.9 K and 9 K for Edimim[FeCl$_4$] and Edimim[FeBr$_4$], respectively, (see the insets of Fig. 7) denoting the existence of long-range magnetic order, with a gradual decrease in the susceptibility of ca. 15%, which is usual for non-oriented antiferromagnets. It is worth mentioning that the replacement of Cl with Br in Edimim[FeX$_4$] leads to an increase in the Néel temperature (T$_N$), favoring stronger magnetic interactions. This agrees with findings in Emim[FeX$_4$] (T$_N$: 4.2 K for X = Cl and 12.5 K for X = Br)[38, 51] and Dimim[FeX$_4$] (T$_N$: 5.6 K for X = Cl and 7.7 K for X = Br) [40, 41] paramagnetic ILs. However, the Néel temperature of the bromide compound is higher than that obtained for Dimim[FeBr$_4$]. This fact goes against our first hypothesis of a smaller chain length of the organic cation causing an increase of the efficiency in the transmission of the magnetic interactions, resulting in an increase in the ordering temperatures in paramagnetic ILs based on tetrahaloferrate ions. On the other hand, χ_m maxima shift to lower temperatures with increasing magnetic field (see Fig. 8), as expected for an AF ordering, and disappear for larger magnetic fields (60 kOe) for Edimim[FeCl$_4$]. However, for Edimim[FeBr$_4$] the maximum in susceptibility does not disappear in the 0-80 kOe range, this field not being strong enough to break the AF ordering. This is an evidence of stronger magnetic couplings, as observed in Dimim[FeBr$_4$].[41]

Fig. 8

Fig. 9 depicts the magnetization as a function of the magnetic field (H) at 2 K for Edimim[FeX$_4$] (X = Cl and Br). The magnetization shows no hysteresis at this temperature, in the ordered state (see inset of Fig. 9), thereby excluding the existence of any ferromagnetic component. Moreover, in the case of Edimim[FeCl$_4$] the magnetization tends to saturate above 40 kOe with a value of ≈ 4.6 μ_B/Fe ion, which is near the expected fully-saturated value of 5 μ_B/Fe for Fe (III) ion. However, for Edimim[FeBr$_4$] the magnetization rises continuously, with an small inflexion near 30 kOe, and does not show saturation up to 85 kOe. In fact, the magnetization value attained in this magnetic field (≈ 2.30 μ_B/Fe ion) is far from the expected fully-saturated value, which confirms a stronger magnetocrystalline anisotropy within this material with respect to the chloride analogue, similar to other analogous paramagnetic ILs based on tetrahaloferrate with 3D ordering[11, 40, 41]. The M(H) curves measured between 2 K and the paramagnetic state (see Fig. S3) allowed us to prepare the Arrott plots (M^2 vs. H/M). A change of regime below 3.0 and 9 K is found in the low temperature region for the chloride and bromide compounds respectively, indicating the appearance of long-range AF order in agreement with the magnetic susceptibility measurements.

Fig. 9

Fig. 10 shows the temperature dependence of the molar heat capacity (C$_P$) for the presented compounds, between 2 and 300 K. In the absence of an external magnetic field, C$_P$ reveals a maximum (ΔC_p= 19 and 8 J/molK) at 2.9 and 8.8 K for Edimim[FeCl$_4$] and Edimim[FeBr$_4$], respectively (see upper insets in Fig. 10). This anomaly reveals a second-order transition and it can be related to the establishment of 3D antiferromagnetic order. The heat capacity measurements in the presence of an applied magnetic field show that the maxima get smaller and shift toward lower temperatures as the field increases. In addition, the magnetic peak of the bromide compound does not disappear for fields larger than 80 kOe, corroborating the presence of the stronger magnetocrystalline anisotropy, as detected in the magnetic susceptibility data.

Fig. 10

Cp increases continuously above the magnetic peak and below 280 K in both compounds due to the phonon contribution. The curves show an inflexion point for T > 280 K, associated with the beginning of the solid-solid transition detected in the calorimetric measurements, (see Fig. 1) near RT. Interestingly, the value at 280 K (≈ 330 J/molK) it is still far from the value derived from the Dulong-Petit law (Cp=675 J/molK at RT) due to the presence of a high number of hydrogen atoms within the imidazolium cation, displaying high excitation energies.[62, 63]

The magnetic contribution to the heat capacity (C_{mag}) of both phases was determined by subtracting the phonon contribution (C_{pho}) up to 270 K, considering a Debye model[64] with the existence of three Debye temperatures (θ) [41]. The highest temperature (θ_1) relates to the n_1 lighter atoms (hydrogen atoms), θ_2 and n_2 corresponds to the medium-weight atoms (C and N), and θ_3 and n_3 to heavier atoms (Fe, Cl or Br); with $n_1+ n_2+ n_3=N$ being N the number of the atoms in the unit cell. The thermal variation of C_{mag} is presented in the lower insets of Fig. 10. The best fit for the experimental data of Edimim[$FeCl_4$] at temperatures higher than 15 K yields θ_1=1840 K, θ_2=315 K, θ_3=99 K, n_1= 17.7, n_2=5.7 and n_3=3.6; similar parameters that was obtained for Edimim[$FeBr_4$]. We should pointing out that although it is a simplified model, it allow to estimate reasonable well the non-magnetic contribution in the low temperature region (T < 20 K) (see low insets of Fig 10). As can be see, C_{mag} progressively increases for Edimim[$FeBr_4$] as the temperature becomes smaller until it reaches the maximum at the onset of the 3D magnetic ordering. Moreover, in Edimim[$FeCl_4$], a shoulder around 10 K suggests low-dimensional ordering[65] or short-range magnetic ordering[66], prior to the establishment of the 3D magnetic ordering. The integral of C_{mag}/T with respect to the temperature, provides the magnetic entropy (see Fig. S4). Both samples show a value near 14.8 J mol^{-1} K^{-1} corresponding with the full entropy $\Delta S=R\cdot\ln((2\cdot5/2)+1)$ (R = 8.31 J/mol K) for a system with high spin d^5 Fe(III) ions, spin S=5/2.

The role of the organic cation in the efficiency of the transmission of the magnetic interactions of paramagnetic ILs can be studied from the analysis of the magnetostructural correlations of the presented compounds and the comparison with the paramagnetic ionic liquid analogues, Dimim[$FeCl_4$] and Dimim[$FeBr_4$], which we have studied in a previous work. The crystal structures of Edimim[$FeCl_4$] and Edimim[$FeBr_4$] at 100 K give no evidence for direct iron-iron interactions. At this temperature, the Fe··Fe distances are 6.547 and 7.053 Å inside a layer (in the a-c plane, respectively) and 8.345 Å in the *b* direction [see Fig S2 (a) and Table 2]. For bromide compound, the iron-iron distances are 6.957 and 7.232 (in plane) and 8.667 Å (along b), respectively [see Fig S2 (b) and Table 3].Therefore, the 3D antiferromagnetic ordering detected by magnetic measurements must take place via super-exchange coupling, the Fe−X···X−Fe (X = Cl and Br) interaction being the main exchange pathway. In addition, the interactions distances between halide and imidazolium (Fig. 5) along the b direction promote a weak orbital coupling between Fe^{+3} ions. Thus, indirect exchange coupling of the type Fe-X··Im···X-Fe, which should be weakest due to the involvement of an imidazolium donor cation (defined as S= ½)[67] inside the magnetic exchange-pathway could be present in these compounds. Moreover, it would seem reasonable to suggest that if the crystal structure of both compounds at 100 K is maintained below T_N, three direct superexchange pathways are detected: i) one magnetic J interplanar interaction ($J1$ or $J\perp$), which gives rise to zig-zag chains forming a ladder structure that runs parallel to the *b* direction ii) two intraplane couplings, $J2$ and $J3$ ($J\|$), which link the iron atoms in linear ferromagnetic chains in the *ac* plane (Table 5). Despite the fact that X···X distances are slightly longer than the sum of the vdw- radii of two halure atoms (see Fig. 3), the data show a remarkable agreement with the contact distances reported in other paramagnetic ILs[44] and metal–organic materials[35, 68] with 3D magnetic ordering that show this type of magnetic coupling. In addition, a decrease of these distances is expected below T_N, due to thermal effects, and hence we cannot rule out indirect superexchange anion-anion interactions (Fe-X···Im···X-Fe)[41]. This mechanism has been proposed for the DImimFeBr$_4$, where the magnetic structure was determined.

Table 5

The strength of the magnetic exchange pathways inside both compounds can be discussed and compared observing the following paramenters: (i) X···X distance, (ii) Fe−X···X−Fe angles and (iii) the Fe−X···X−Fe torsion angle (τ) (Table 5). Comparing the X···X distances, the interplanar values (J*1*) (4.171 and 4.095 Å for Cl and Br, respectively) are larger than the intraplane interactions (J*2* and J*3*) [4.025 (lowest distance of J2) and 3.936 for Cl and 3.985 and 4.053 Å for Br). For (ii) and (iii) parameters, the intraplane interactions (J*2* and J*3*) show a mixture of exchange angles: Fe–X···X, between 138.21 and 158.02º and X···X–Fe, from 78.55º and 108.18º, with τ ranging from 34.15 to 168.57º. However, J*1* displays a nearly linear combination of Fe–X···X and X···X – Fe angles (from 168.90 to 152.65 º) with τ = 70.38 and 84.34º for Cl and Br, respectively. Thus, the interplanar magnetic interaction is found to be stronger than the intraplanar ones in both compounds, according to the rule that shorter halide-halide distances, larger Fe−X···X−Fe angles, and Fe−X···X−Fe torsion angles near 90º correspond to stronger magnetic exchange constants;[35] which agrees with the reports on Dimim[FeCl$_4$] and Dimim[FeBr$_4$][41] analogues.

The exchange couplings between the Fe^{3+} ions can also be quantitatively analyzed from the macroscopic experimental parameters. The best model to describe the magnetic susceptibility data includes a combination of a modified expression of the classical spin ladder-like chain (1D) for interplanar interactions together with a mean-field term with spin 5/2, to account for the intraplanar ones (2D).[69]

$$\chi_m = \frac{1}{3}\chi_\perp + \frac{2}{3}\chi_\parallel$$

where the linear chain model for the interplanar exchange interaction is given by a modified [70] Bonner and Fisher model[71] and the susceptibility

$$\chi_\perp = \frac{NS(S+1)}{3kT}\mu_B^2 g^2 \frac{1+u(K)}{1-u(K)} \qquad (1)$$

with

$$u(K) = \coth K - 1/K$$

$$K = -2J_\perp S(S+1)/kT$$

and $J_\perp$ defined positive for AF coupling, considering $\mathcal{H}_{ex} = \sum_{nn} 2J\mathbf{S_i}\cdot\mathbf{S_j}$. In addition, the magnetic susceptibility for the 2D AF framework, $\chi_\parallel$ for S=5/2 is given by the Rushbrook and Wood expression[72]

$$\chi_\parallel = \left(\frac{N\mu_B^2 g^2 S(S+1)}{3kT}\right)\cdot(1 - 23.333x + 147.78x^2 - 405.48x^3 + 8171.3x^4 - 6461.8x^5 - 158110x^6)^{-1} \qquad (2)$$

where $x = -J_\parallel/kT$, with $J_\parallel$ positive for AF coupling.

The least-squares fit of the experimental data from 2 to 300 K [solid line in Fig. 11], yields g=2.00 and 2.006, $J_\perp$= -0.050 and -0.195 K and $J_\parallel$=0.033 and 0.145 K. The proposed approach can be valuable in the absence of a more realistic mode even though the quantitative analysis of the exchange couplings should consider the Fe-X··Im··X-Fe exchange magnetic coupling. The estimated exchange parameters show that the Fe-X···X-Fe interactions along the *b* axis are the strongest. In addition, the least-squares fit of the experimental data yields weaker magnetic exchange coupling for the chloride compound, which confirms the macroscopic magnetic data.

Fig. 11

Finally, it was supposed the bigger the imidazolium ion size on paramagnetic ionic liquids based on tetrahaloferrate ions, the weaker superexchange magnetic pathways, due to a larger distances between the iron-iron. However, comparison with Dimim[$FeCl_4$][40] (5.6 K) and Dimim[$FeBr_4$][41] (7.7 K) shows lower T_N in the chloride compound (2.9 K) whereas it is higher for the bromide (9K). On one hand, Fe···Fe distances in Dimim[$FeBr_4$][41] are shorter; At 10 K they are 6.74 and 6.76 Å inside a layer and 8.57 Å between the layers. For Edimim[$FeBr_4$] at 100 K ,are 6.957 and 7.232 and 8.667 Å, respectively. On the other hand, the higher T_N detected in Edimim[$FeBr_4$] cannot be attributed to the geometrical factor of non-bonding interactions neither. Both bromide compounds, Dimim[$FeBr_4$] and Edimim[$FeBr_4$], show an almost linear coupling and out of-plane magnetic exchange angles in interplane and intraplane magnetic interactions, respectively with similar halide-halide distances. Thus, this enhancement of the T_N with a bigger imidazolium cation in the bromide compounds will be attributed to the existence of a higher spin delocalization of iron atoms in the metal complex ions, $[FeBr_4]^-$, which favors the magnetic couplings.[40, 41] This results represents a new evidence of the relative importance of the spin density delocalization of the metal complex anion, which explains this higher efficiency in transmitting the magnetic interaction.

Conclusion

Two novel 3D magnetic correlated ILs based on imidazolium cation and tetrahaloferrate anion, namely Edimim[$FeCl_4$] and Edimim[$FeBr_4$], have been synthetized by solid-phase synthesis exhibiting melting points of 320 and 355 K for Cl and Br, respectively. The chloride compound, characterized by synchrotron X-ray powder diffraction at 100K, crystallizes in the monoclinic space group $P2_1/n$. For the bromide composite, the crystal structure shows a monoclinic phase $P2_1$, characterized from single crystal X-ray diffraction at 100 K. Their frameworks, projected along b direction, are formed by layers of $[Edimim]^+$ cations and $[FeBr_4]^-$ anions which change orientation from layer to layer, stacked upon one another in a 3D manner displaying three types of non-covalent interactions: hydrogen bonding, anion-π, and halide-halide. Raman measurements of both compounds at RT corroborate the presence of $[FeX_4]^-$ (X = Cl and Br) and the gauche (non-planar) equilibrium conformation of the imidazolium cation with respect to NCC angle of the ethyl group. Magnetic studies of both compounds using magnetic susceptibility, magnetization and heat capacity measurements, show predominantly AF interactions and 3D magnetic ordering below 2.9 and 9 K for Edimim[$FeCl_4$] and Edimim[$FeBr_4$], respectively; together with the presence of stronger magnetocrystalline anisotropy in the latter. The magneto-structural correlations in both compounds give evidence that the 3D magnetic ordering mainly takes place via Fe-X···X-Fe interactions (X = Cl and Br), displaying a higher superexchange magnetic interaction between the planes. A comparative study with Dimim[FeX_4] (X = Cl and Br) shows a lower T_N in the chloride compound whereas it is higher for the bromide composite. This issue discards the hypothesis that the size of the cation play the most important role in the strength of the magnetic exchange pathways of the paramagnetic ionic liquids based on tetrahaloferrate anion and imidazolium cation.

Acknowledgments

Financial support from the Spanish Ministerio de Ciencia e Innovación (Projects MAT2011-27573-C04) and Becas Iberoamericas Jóvenes Profesores Investigadores, 2011, Santander Universidades is acknowledged. The authors gratefully acknowledge the MALTA Consolider Ingenio 2010 (Ref. CSD2007-00045). IH acknowledges funding from the EU FP7 (Marie Curie-CIG 303535). X-Ray Synchrotron powder diffraction experiments were performed at BL04 beamline of the ALBA Synchrotron (proposal id 2013100582).

Associated content

Supporting Information display crystallographic information, CIF data, and supplementary magnetic measurements.

References

1. T. Welton, *Chemical Reviews*, 1999, **99**, 2071-2084.
2. E. Santos, J. Albo and A. Irabien, *RSC Advances*, 2014, **4**, 40008-40018.
3. T. Torimoto, T. Tsuda, K.-i. Okazaki and S. Kuwabata, *Advanced Materials*, 2010, **22**, 1196-1221.
4. M. Dobbelin, V. Jovanovski, I. Llarena, L. J. Claros Marfil, G. Cabanero, J. Rodriguez and D. Mecerreyes, *Polymer Chemistry*, 2011, **2**, 1275-1278.
5. B. Mallick, B. Balke, C. Felser and A.-V. Mudring, *Angewandte Chemie International Edition*, 2008, **47**, 7635-7638.
6. M. Okuhata, Y. Funasako, K. Takahashi and T. Mochida, *Chemical Communications*, 2013, **49**, 7662-7664.
7. A. Branco, L. C. Branco and F. Pina, *Chemical Communications*, 2011, **47**, 2300-2302.
8. A.-V. Mudring, A. Babai, S. Arenz, R. Giernoth, K. Binnemans, K. Driesen and P. Nockemann, *Journal of Alloys and Compounds*, 2006, **418**, 204-208.
9. S. Hayashi and H.-o. Hamaguchi, *Chemistry Letters*, 2004, **33**, 1590-1591.
10. I. de Pedro, D. P. Rojas, J. Albo, P. Luis, A. Irabien, J. A. Blanco and J. Rodriguez Fernandez, *Journal of Physics-Condensed Matter*, 2010, **22,** 29006.
11. I. de Pedro, D. P. Rojas, J. A. Blanco and J. Rodriguez Fernandez, *Journal of Magnetism and Magnetic Materials*, 2011, **323**, 1254-1257.
12. P. De Vreese, N. R. Brooks, K. Van Hecke, L. Van Meervelt, E. Matthijs, K. Binnemans and R. Van Deun, *Inorganic Chemistry*, 2012, **51**, 4972-4981.
13. S. Pitula and A. V. Mudring, *Chemistry-A European Journal*, 2010, **16**, 3355-3365.
14. R. E. Del Sesto, T. M. McCleskey, A. K. Burrell, G. A. Baker, J. D. Thompson, B. L. Scott, J. S. Wilkes and P. Williams, *Chemical Communications*, 2008, **0**, 447-449.
15. T. Peppel, M. Köckerling, M. Geppert-Rybczyńska, R. V. Ralys, J. K. Lehmann, S. P. Verevkin and A. Heintz, *Angewandte Chemie International Edition*, 2010, **49**, 7116-7119.
16. S. Tang, A. Babai and A.-V. Mudring, *Angewandte Chemie International Edition*, 2008, **47**, 7631-7634.
17. K. Binnemans, *Chemical reviews*, 2007, **107**, 2592-2614.
18. K. Tanaka, F. Ishiguro and Y. Chujo, *Journal of the American Chemical Society*, 2010, **132**, 17649-17651.
19. C.-X. Miao, J.-Q. Wang, B. Yu, W.-G. Cheng, J. Sun, S. Chanfreau, L.-N. He and S.-J. Zhang, *Chemical Communications*, 2011, **47**, 2697-2699.
20. O. Nacham, K. D. Clark, H. Yu and J. L. Anderson, *Chemistry of Materials*, 2015, **27**, 923-931.
21. P. Brown, C. P. Butts, J. Eastoe, E. Padron Hernandez, F. L. d. A. Machado and R. J. de Oliveira, *Chemical Communications*, 2013, **49**, 2765-2767.
22. M. Okuno, H. Hamaguchi and S. Hayashi, *Appl. Phys. Lett.*, 2006, **89**, 132506.
23. E. Santos, J. Albo, A. Rosatella, C. A. M. Afonso and Á. Irabien, *Journal of Chemical Technology & Biotechnology*, 2014, **89**, 866-871.
24. P. Brown, A. Bushmelev, C. P. Butts, J. Cheng, J. Eastoe, I. Grillo, R. K. Heenan and A. M. Schmidt, *Angewandte Chemie International Edition*, 2012, **51**, 2414-2416.

25. K. D. Clark, O. Nacham, H. Yu, T. Li, M. M. Yamsek, D. R. Ronning and J. L. Anderson, *Analytical chemistry*, 2015, **87**, 1552-1599.
26. A. H. Mohammad Fauzi, N. A. S. Amin and R. Mat, *Applied Energy*, 2014, **114**, 809-818.
27. R. Giernoth, A. Bröhl, M. Brehm and Y. Lingscheid, *Journal of Molecular Liquids*, 2014, **192**, 55-58.
28. S. Zhang, J. Wang, X. Lu and Q. Zhou, *Structures and Interactions of Ionic Liquids*, Springer, 2014.
29. K. Fumino and R. Ludwig, *Journal of Molecular Liquids*, 2014, **192**, 94-102.
30. J. Dupont, *Accounts of Chemical Research*, 2011, **44**, 1223-1231.
31. R. P. Matthews, T. Welton and P. Hunt, *Physical Chemistry Chemical Physics*, 2015, **17**, 14437-14453.
32. J. Dupont, *Journal of the Brazilian Chemical Society*, 2004, **15**, 341-350.
33. S. Saha, S. Hayashi, A. Kobayashi and H.-o. Hamaguchi, *Chem. Lett.*, 2003, **32**, 740-741.
34. H. Weingärtner, *Angewandte Chemie International Edition*, 2008, **47**, 654-670.
35. R. Bertani, P. Sgarbossa, A. Venzo, F. Lelj, M. Amati, G. Resnati, T. Pilati, P. Metrangolo and G. Terraneo, *Coordination Chemistry Reviews*, 2010, **254**, 677-695.
36. A. Frontera, P. Gamez, M. Mascal, T. J. Mooibroek and J. Reedijk, *Angewandte Chemie International Edition*, 2011, **50**, 9564-9583.
37. Y. Yoshida, A. Otsuka, G. Saito, S. Natsume, E. Nishibori, M. Takata, M. Sakata, M. Takahashi and T. Yoko, *Bulletin of the Chemical Society of Japan*, 2005, **78**, 1921-1928.
38. Y. Yoshida and G. Saito, *Journal of Materials Chemistry*, 2006, **16**, 1254-1262.
39. A. García-Saiz, I. de Pedro, J. A. Blanco, J. González and J. R. Fernández, *The Journal of Physical Chemistry B*, 2013, **117**, 3198-3206.
40. A. García-Saiz, P. Migowski, O. Vallcorba, J. Junquera, J. A. Blanco, J. A. González, M. T. Fernández-Díaz, J. Rius, J. Dupont, J. Rodríguez Fernández and I. de Pedro, *Chemistry – A European Journal*, 2014, **20**, 72-76.
41. A. Garcia-Saiz, I. de Pedro, P. Migowski, O. Vallcorba, J. Junquera, J. A. Blanco, O. Fabelo, D. Sheptyakov, J. C. Waerenborgh, M. T. Fernandez-Diaz, J. Rius, J. Dupont, J. A. Gonzalez and J. R. Fernandez, *Inorg Chem*, 2014, **53**, 8384-8396.
42. S. Hayashi, S. Saha and H. Hamaguchi, *IEEE Trans. Magn.*, 2006, **42**, 12.
43. H. Tokuda, K. Hayamizu, K. Ishii, M. A. B. H. Susan and M. Watanabe, *The Journal of Physical Chemistry B*, 2005, **109**, 6103-6110.
44. A. Boultif and D. Louër, *Journal of Applied Crystallography*, 2004, **37**, 724-731.
45. O. Vallcorba, J. Rius, C. Frontera, I. Peral and C. Miravitlles, *Journal of Applied Crystallography*, 2012, **45**, 844-848.
46. O. Vallcorba, J. Rius, C. Frontera and C. Miravitlles, *Journal of Applied Crystallography*, 2012, **45**, 1270-1277.
47. I. J. Bruno, J. C. Cole, M. Kessler, J. Luo, W. S. Motherwell, L. H. Purkis, B. R. Smith, R. Taylor, R. I. Cooper and S. E. Harris, *Journal of chemical information and computer sciences*, 2004, **44**, 2133-2144.
48. Bruker, *SADABS, Bruker AXS Inc., Madison, Wisconsin, USA*, (2001).
49. G. Sheldrick, *Acta Crystallographica Section A*, 2008, **64**, 112-122.
50. D. Appleby, C. L. Hussey, K. R. Seddon and J. E. Turp, *Nature*, 1986, **323**, 614-616.
51. Y. Yoshida and G. Saito, *Journal of Materials Chemistry*, 2006, **16**, 1254-1262.
52. C. Zhong, T. Sasaki, A. Jimbo-Kobayashi, E. Fujiwara, A. Kobayashi, M. Tada and Y. Iwasawa, *Bulletin of the Chemical Society of Japan*, 2007, **80**, 2365-2374.
53. Y. Umebayashi, T. Fujimori, T. Sukizaki, M. Asada, K. Fujii, R. Kanzaki and S.-i. Ishiguro, *The Journal of Physical Chemistry A*, 2005, **109**, 8976-8982.
54. J. Estager, J. Holbrey and M. Swadźba-Kwaśny, *Chemical Society Reviews*, 2014, **43**, 847-886.
55. L. M. Salonen, M. Ellermann and F. Diederich, *Angewandte Chemie International Edition*, 2011, **50**, 4808-4842.

56. B. P. Hay and R. Custelcean, *Crystal Growth & Design*, 2009, **9**, 2539-2545.
57. J.-Y. Kim, J.-T. Kim, E.-A. Song, Y.-K. Min and H.-o. Hamaguchi, *Macromolecules*, 2008, **41**, 2886-2889.
58. P. Larkin, *Infrared and Raman spectroscopy; principles and spectral interpretation*, Elsevier, 2011.
59. R. Ozawa, S. Hayashi, S. Saha, A. Kobayashi and H.-o. Hamaguchi, *Chemistry Letters*, 2003, **32**, 948-949.
60. N. E. Heimer, R. E. Del Sesto, Z. Meng, J. S. Wilkes and W. R. Carper, *Journal of molecular liquids*, 2006, **124**, 84-95.
61. I. de Pedro, A. Garcia-Saiz, J. Gonzalez, I. Ruiz de Larramendi, T. Rojo, C. A. M. Afonso, S. P. Simeonov, J. C. Waerenborgh, J. A. Blanco, B. Ramajo and J. R. Fernandez, *Physical Chemistry Chemical Physics*, 2013, **15**, 12724-12733.
62. I. de Pedro, J. M. Rojo, J. Rodríguez Fernández, M. T. Fernández-Díaz and T. Rojo, *Physical Review B*, 2010, **81**, 134431.
63. I. de Pedro, J. M. Rojo, J. Rodriguez Fernandez, J. Sanchez Marcos, M. T. Fernandez-Diaz and T. Rojo, *Journal of Solid State Chemistry*, 2012, **188**, 1-10.
64. P. Debye, *Annalen der Physik*, 1912, **344**, 789-839.
65. I. De Pedro, J. M. Rojo, J. Rius, O. Vallcorba, I. Ruiz De Larramendi, J. Rodríguez Fernández, L. Lezama and T. Rojo, *Inorganic Chemistry*, 2012, **51**, 5246-5256.
66. I. De Pedro, J. M. Rojo, J. Rodríguez Fernández, L. Lezama and T. Rojo, *European Journal of Inorganic Chemistry*, 2010, **17**, 2514-2522.
67. J. Glerup, P. A. Goodson, D. J. Hodgson and K. Michelsen, *Inorganic Chemistry*, 1995, **34**, 6255-6264.
68. J. Campo, J. Luzón, F. Palacio, G. J. McIntyre, A. Millán and A. R. Wildes, *Physical Review B*, 2008, **78**, 054415.
69. J. McElearney, S. Merchant and R. Carlin, *Inorganic Chemistry*, 1973, **12**, 906-908.
70. G. R. Wagner and S. A. Friedberg, *Physics Letters*, 1964, **9**, 11-13.
71. J. C. Bonner and M. E. Fisher, *Physical Review*, 1964, **135**, A640-A658.
72. G. S. Rushbrooke and P. J. Wood, *Molecular Physics*, 1958, **1**, 257-283.

Figure and Table Captions

Fig. 1. DSC-thermogram of (a) Edimim[$FeCl_4$] and (b) Edimim[$FeBr_4$]. Black line: 1st cooling cycle; blue line: 2nd heating cycle. Heating rate 10 K/min. The insets show the TGA curves of Edimim[$FeCl_4$] and Edimim[$FeBr_4$], respectively recorded in inert atmosphere.

Fig. 2. Crystal packing in the *bc* plane of (a) Edimim[$FeCl_4$] and (b) Edimim[$FeBr_4$] crystal structures at 100 K. Orange: iron, green: chloride, gold: bromine, grey: carbon and blue: nitrogen. H atoms are omitted for clarity.

Fig. 3. Schematic view of the halide-halide interactions (dashed lines; possible magnetic exchange pathways) for (a) Edimim[$FeCl_4$] via Fe−Cl···Cl−Fe bridges and (b) Edimim[$FeBr_4$] via Fe−Br···Br−Fe bridges. Distance units in Å.

Fig. 4. Hydrogen-bonding network in (a) Edimim[$FeCl_4$] and (b) Edimim[$FeBr_4$]. H—X (X =Cl and Br) contacts up to 3.05 and 3.15 Å are plotted with dashed lines. Distance units in Å.

Fig. 5. Schematic view of the cation and anion arrangement (dashed lines) within the main contact distances for (a) Edimim[$FeCl_4$] and (b) Edimim[$FeBr_4$]. Distance units in Å.

Fig. 6. Raman spectra of Edimim[$FeCl_4$] between 100 and 3300 cm^{-1} at 300 K. The inset shows the low and the high energy region of Raman spectra of Edimim[$FeCl_4$] and Edimim[$FeBr_4$] at 300 K.

Fig. 7. Temperature dependence of the molar susceptibility (χ_m) and $1/\chi_m$ measured at 1 kOe for (a) Edimim[$FeCl_4$]; (b) Edimim[$FeBr_4$]. The solid red lines are the fit according to Curie-Weiss law. The insets show an enlargement of the low temperature region of (χ_m).

Fig. 8. Low temperature ZFC magnetic susceptibility at different applied magnetic fields for (a) Edimim[$FeCl_4$]; (b) Edimim[$FeBr_4$].

Fig. 9. Magnetization vs. applied magnetic field for Edimim[$FeCl_4$] and Edimim[$FeBr_4$] at 2 K.

Fig. 10. Specific heat of (a) Edimim[$FeCl_4$] and (b) Edimim[$FeBr_4$] between 2 and 300 K. Lower inset shows the experimental data (black full dots), estimated phonon contribution (red dashed line) and magnetic contribution (blue full dots). The upper inset is the specific heat at different applied magnetic field ($H \leq 85$ kOe).

Fig. 11. Temperature dependence of χ_m (black circles) for (a) Edimim[$FeCl_4$] and (b) Edimim[$FeBr_4$] measured under 1 kOe. The solid red lines are the fit according to Equation (2).

Fig. S1. Observed (red points) and calculated (blank solid line) powder diffraction patterns for Edimim[$FeCl_4$] synchrotron powder X-ray data at 100 K. Positions of the Bragg reflections are represented by vertical bars. The observed-calculated pattern difference is given at the bottom of the figure.

Fig. S2. Experimental Iron-Iron distance inside the crystal structure of (a) Edimim[$FeCl_4$] and (b) Edimim[$FeBr_4$] at 100K.

Fig. S.3. Arrott plots for (a) Edimim[$FeCl_4$] and (b) Edimim[$FeBr_4$].

Fig. S.4. The magnetic entropy variation as a function of temperature for (a) Edimim[$FeCl_4$] and (b) Edimim[$FeBr_4$].

Table 1. Crystallographic data and structure refinement for Edimim[$FeCl_4$] and Edimim[$FeBr_4$] at 100K.

Table 2. Most relevant interatomic distances in the crystal structure of Edimim[$FeCl_4$] at 100K.

Table 3. Most relevant interatomic distances in the crystal structure of Edimim[$FeBr_4$] at 100K.

Table 4. Vibrational assignment (cm^{-1}) of Edimim[$FeCl_4$] at room temperature.

Table 5. Selected geometrical parameters, bond lengths (Å) and angles (º) (experimental at 100 K) related to the possible magnetic exchange pathways for Edimim[$FeCl_4$] and Edimim[$FeBr_4$].

Table S1. Final refined positional coordinates from synchrotron powder X Ray diffraction pattern of Edimim[$FeCl_4$] at 100 K.

Table S2. Final refined positional coordinates obtained from X Ray single crystal diffraction of Edimim[$FeBr_4$] at 100 K.

Table S3. Anisotropic displacement parameters ($Å^2 x10^3$) for Edimim[$FeBr_4$]. The anisotropic displacement factor exponent takes the form: $-2\pi^2[\ h^2 a^{*2} U_{11} + ... + 2\ h\ k\ a^*\ b^*\ U_{12}\ ]$. U(eq) is defined as one third of the trace of the orthogonalized U_{ij} tensor.

Figures

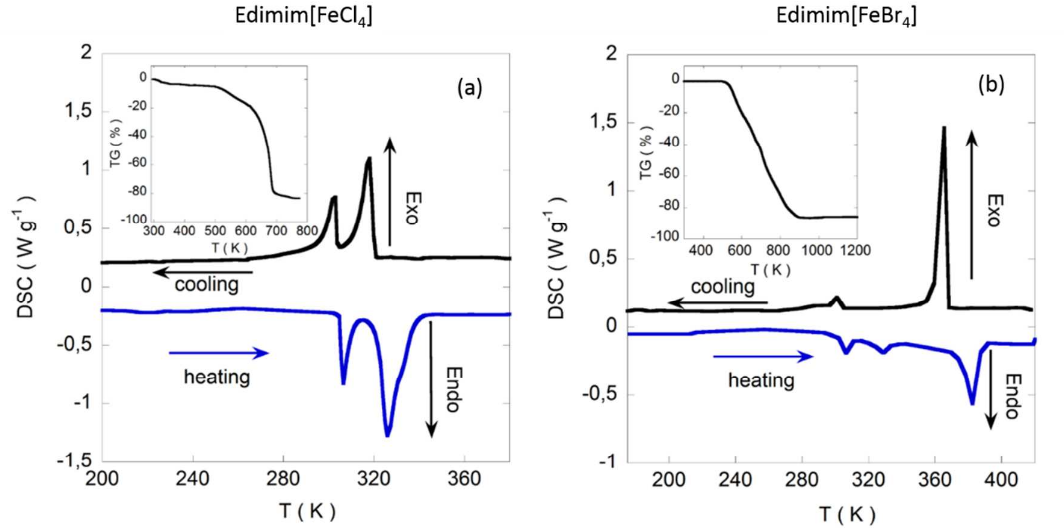

Fig. 1

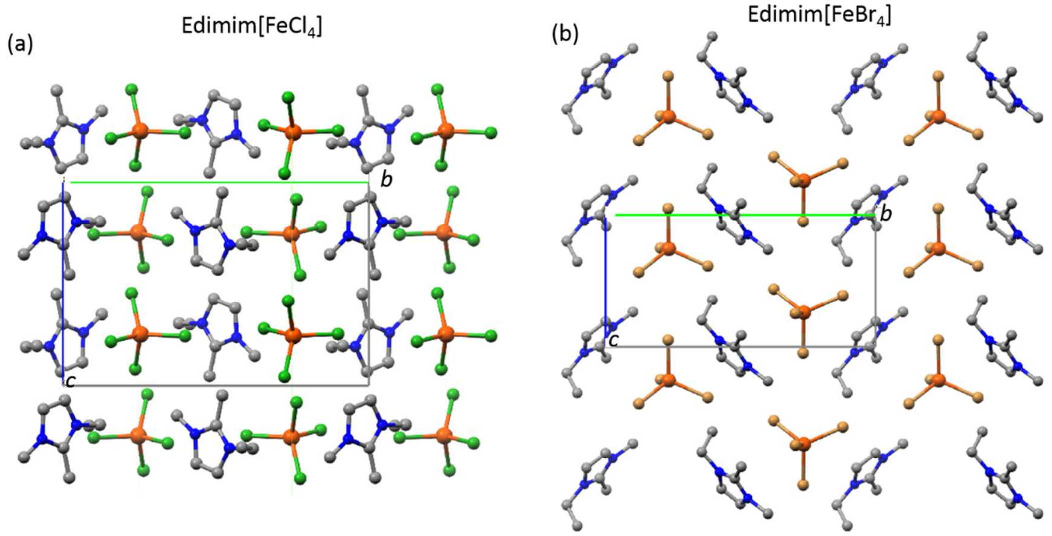

Fig. 2

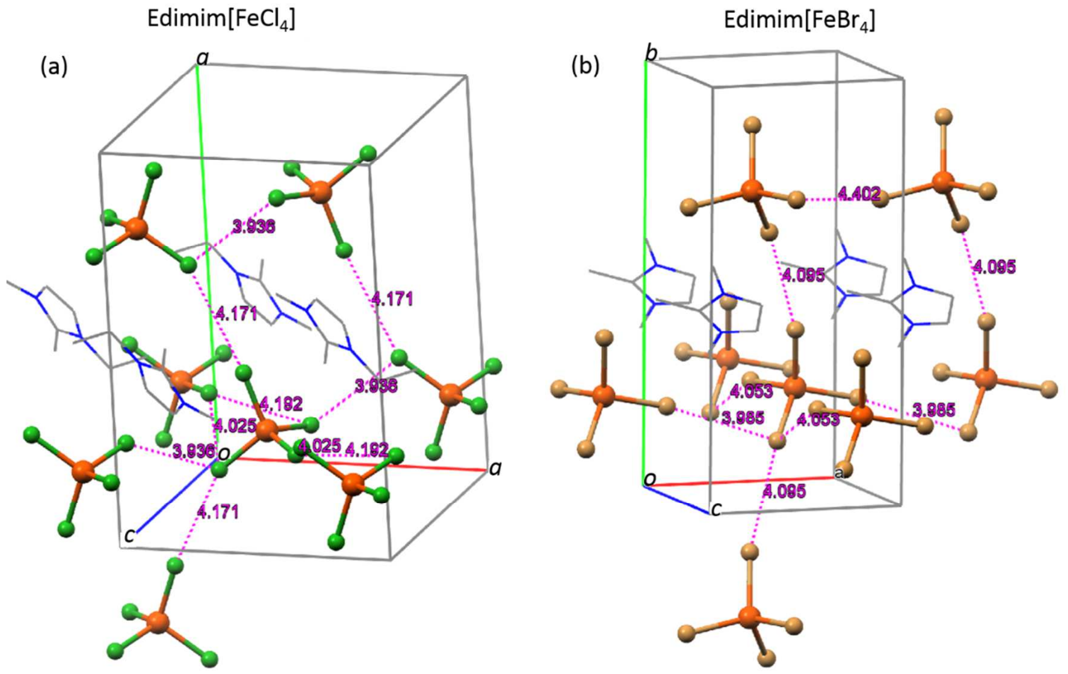
Edimim[FeCl$_4$]
(a)
a
3.936
4.171
4.171
3.936
4.192
4.025
3.936
o
4.025
4.192
a
c
4.171
Edimim[FeBr$_4$]
(b)
b
4.402
4.095
4.095
4.053
3.985
4.053
3.985
o
a
c
4.095

Fig. 3

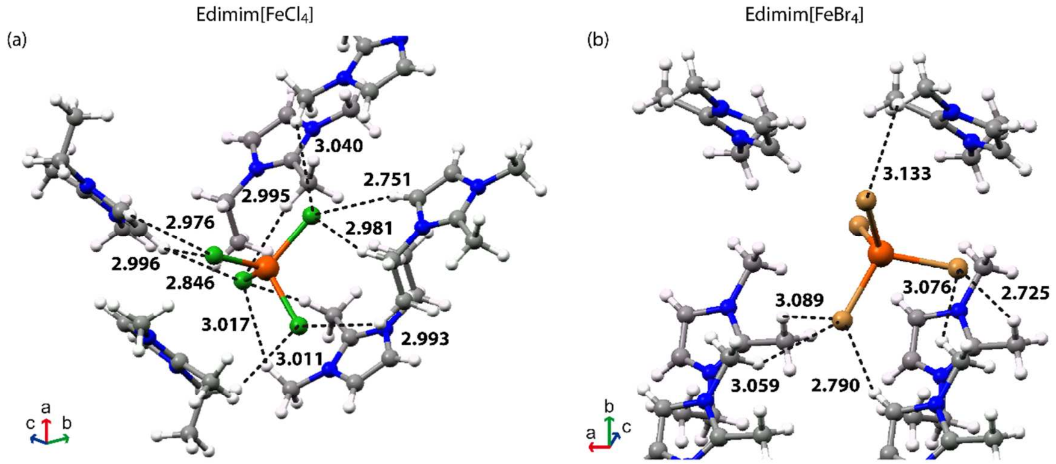
Edimim[FeCl$_4$]
(a)
3.040
2.751
2.995
2.976
2.981
2.996
2.846
3.017
2.993
3.011
a
c
b
Edimim[FeBr$_4$]
(b)
3.133
3.089
3.076
2.725
3.059
2.790
b
a
c

Fig. 4

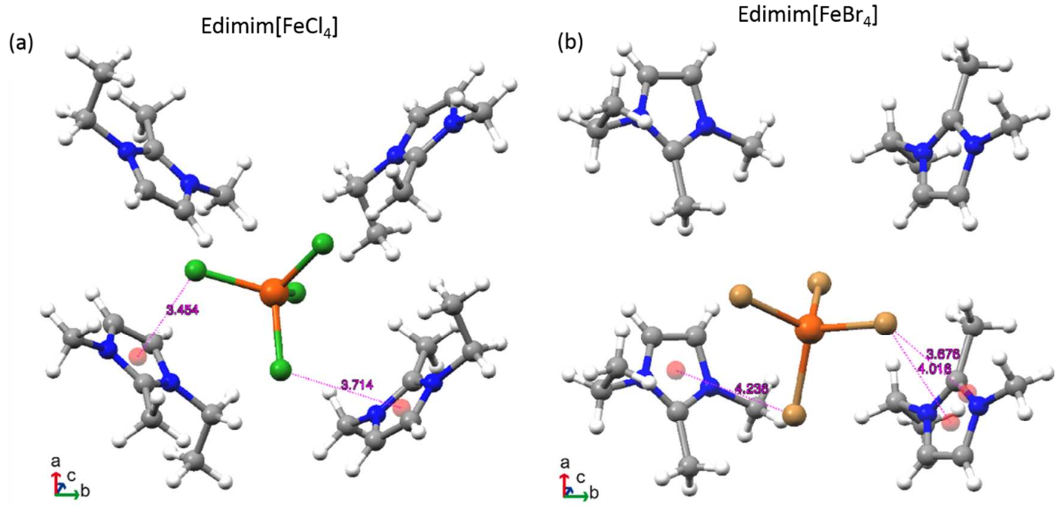
Edimim[FeCl$_4$]
(a)
3.454
3.714
a
c
b
Edimim[FeBr$_4$]
(b)
3.676
4.016
4.236
a
c
b

Fig. 5

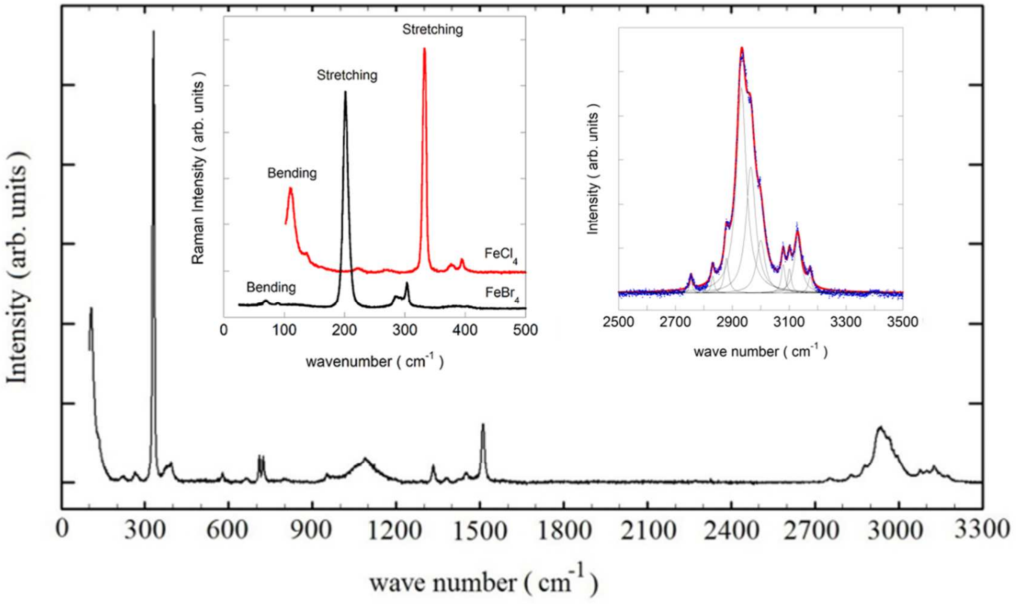
Intensity (arb. units)
0
300
600
900
1200
1500
1800
2100
2400
2700
3000
3300
wave number (cm^{-1})
Raman Intensity (arb. units)
Stretching
Stretching
Bending
Bending
FeCl$_4$
FeBr$_4$
0
100
200
300
400
500
wavenumber (cm^{-1})
Intensity (arb. units)
2500
2700
2900
3100
3300
3500
wave number (cm^{-1})

Fig. 6

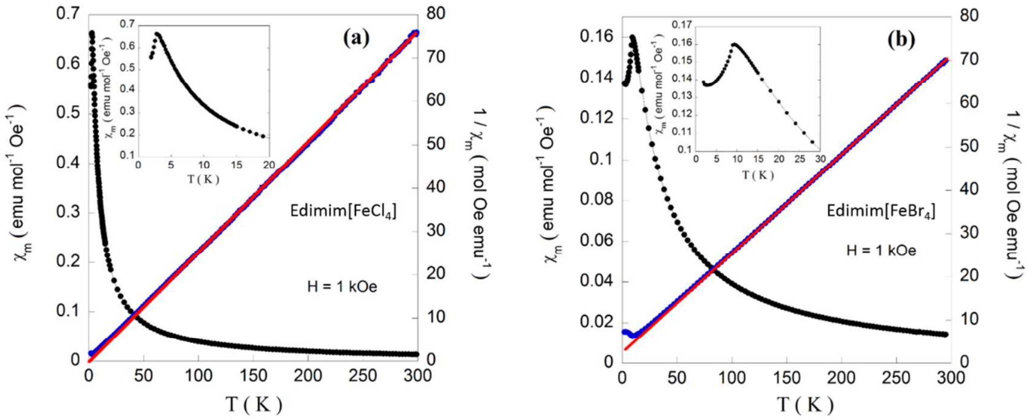
(a)
Edimim[FeCl4]
H = 1 kOe
χm (emu mol-1 Oe-1)
1 / χm (mol Oe emu-1)
T (K)
0.7
0.6
0.5
0.4
0.3
0.2
0.1
0
80
70
60
50
40
30
20
10
0
50
100
150
200
250
300
(b)
Edimim[FeBr4]
H = 1 kOe
0.16
0.14
0.12
0.1
0.08
0.06
0.04
0.02

Fig. 7

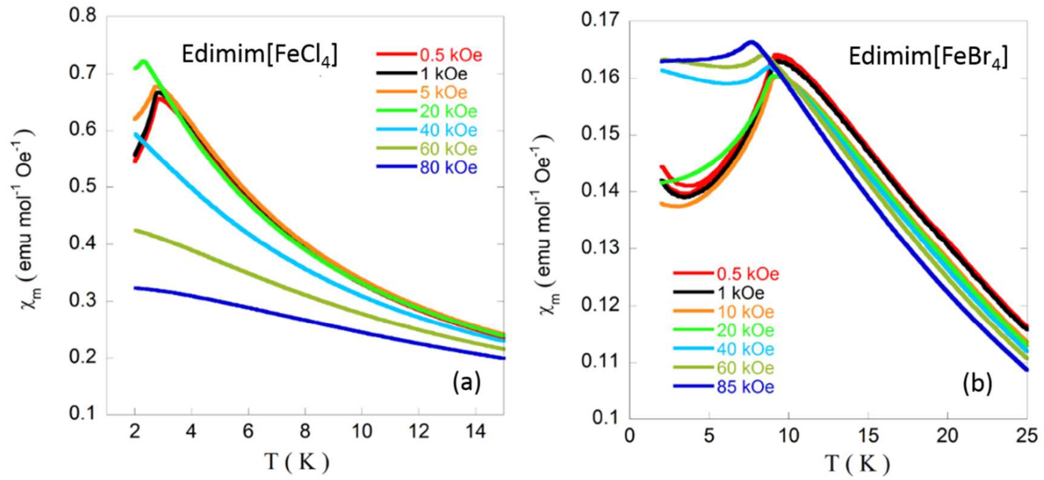
Edimim[FeCl4]
0.5 kOe
1 kOe
5 kOe
20 kOe
40 kOe
60 kOe
80 kOe
(a)
χm (emu mol-1 Oe-1)
T (K)
0.8
0.7
0.6
0.5
0.4
0.3
0.2
0.1
2
4
6
8
10
12
14
Edimim[FeBr4]
0.5 kOe
1 kOe
10 kOe
20 kOe
40 kOe
60 kOe
85 kOe
(b)
0.17
0.16
0.15
0.14
0.13
0.12
0.11
0.1
0
5
10
15
20
25

Fig. 8

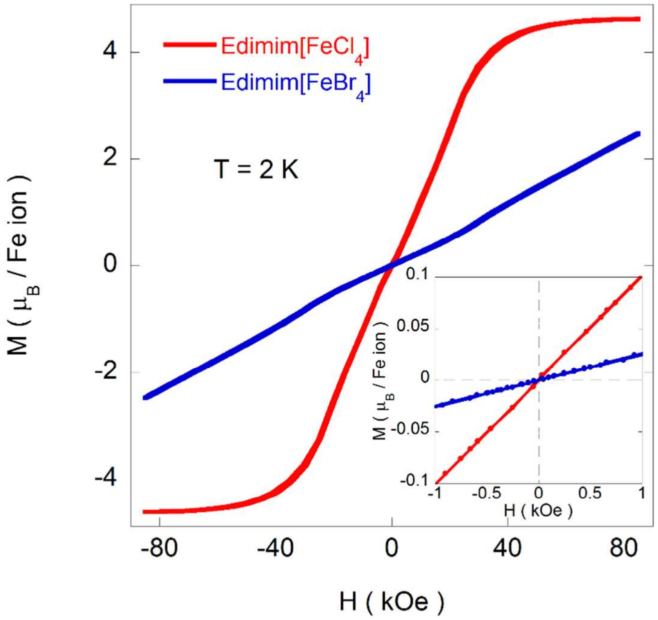
Edimim[FeCl$_4$]
Edimim[FeBr$_4$]
T = 2 K
M (μ$_B$ / Fe ion)
H (kOe)
M (μ$_B$ / Fe ion)
H (kOe)
4
2
0
-2
-4
-80
-40
0
40
80
0.1
0.05
0
-0.05
-0.1
-1
-0.5
0
0.5
1

Fig. 9

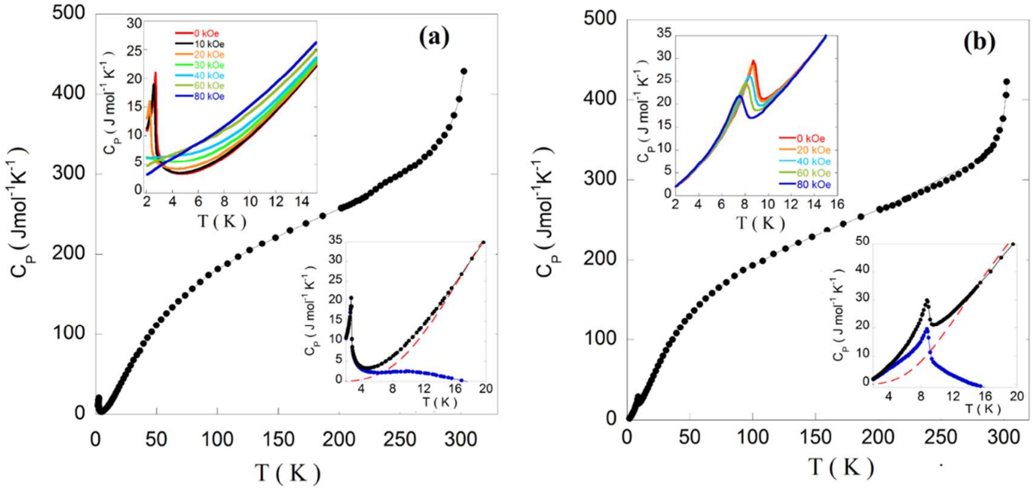
(a)
(b)
C$_p$ (Jmol^{-1}K^{-1})
T (K)
C$_p$ (J mol^{-1} K^{-1})
0 kOe
10 kOe
20 kOe
30 kOe
40 kOe
60 kOe
80 kOe
500
400
300
200
100
0
0
50
100
150
200
250
300

Fig. 10

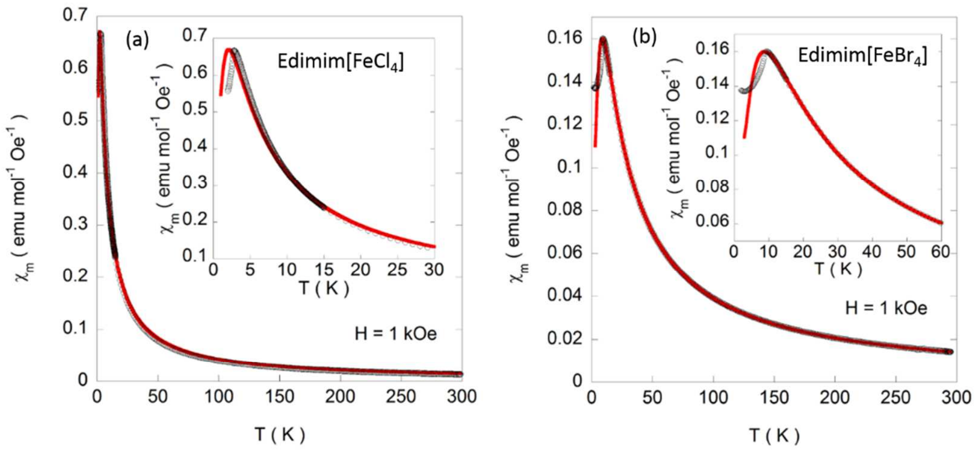

Fig. 11

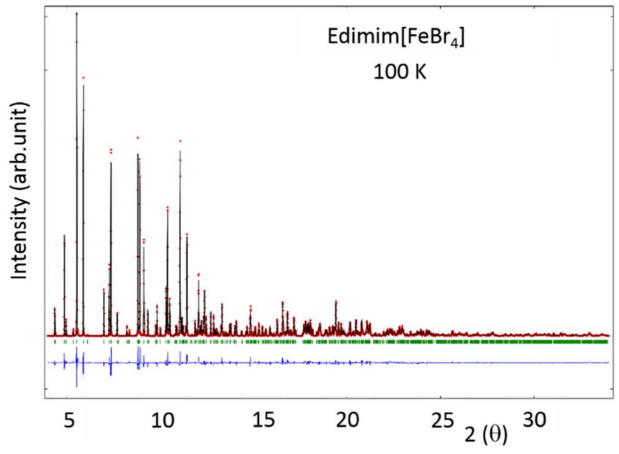

Fig S1

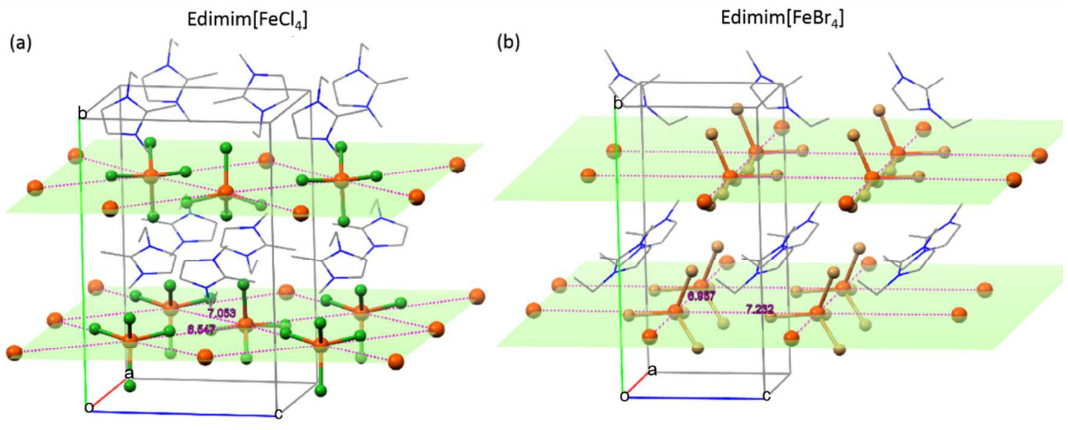

Fig S2

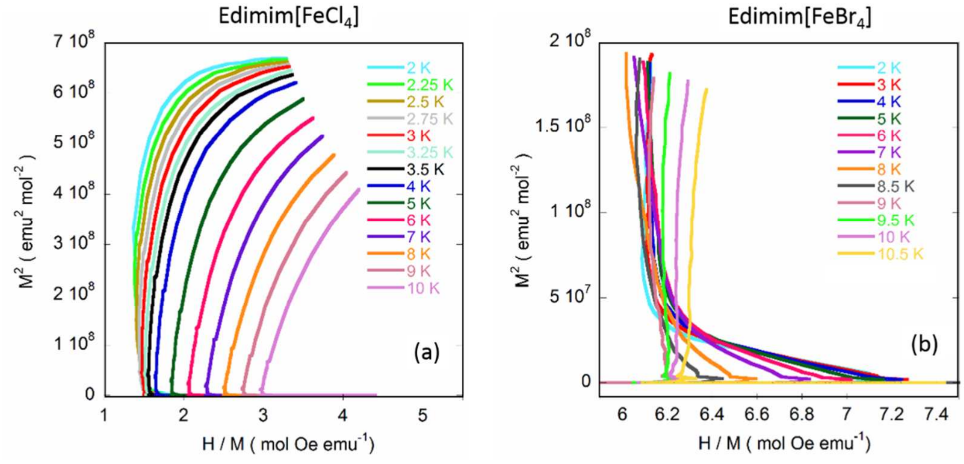

Edimim[FeCl$_4$]
7 10^8
6 10^8
5 10^8
4 10^8
3 10^8
2 10^8
1 10^8
0
M^2 (emu^2 mol^{-2})
1
2
3
4
5
H / M (mol Oe emu^{-1})
2 K
2.25 K
2.5 K
2.75 K
3 K
3.25 K
3.5 K
4 K
5 K
6 K
7 K
8 K
9 K
10 K
(a)
Edimim[FeBr$_4$]
2 10^8
1.5 10^8
1 10^8
5 10^7
0
M^2 (emu^2 mol^{-2})
6
6.2
6.4
6.6
6.8
7
7.2
7.4
H / M (mol Oe emu^{-1})
2 K
3 K
4 K
5 K
6 K
7 K
8 K
8.5 K
9 K
9.5 K
10 K
10.5 K
(b)

Fig. S3

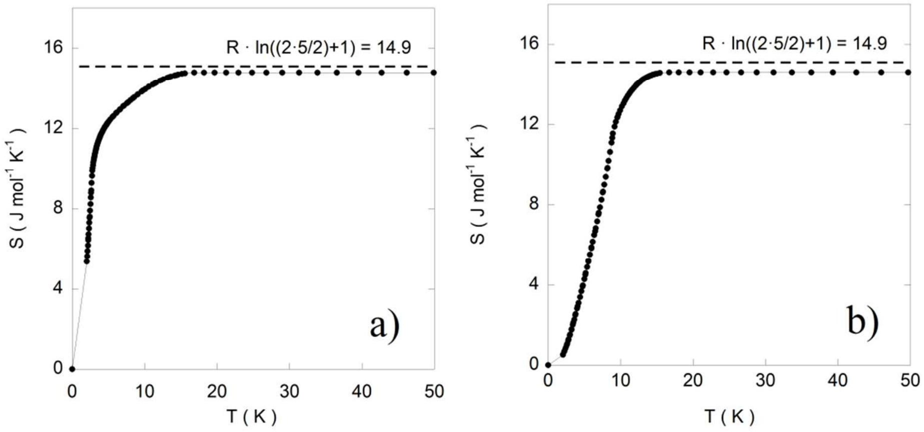

16
12
8
4
0
S (J mol^{-1} K^{-1})
R · ln((2·5/2)+1) = 14.9
a)
0
10
20
30
40
50
T (K)
16
12
8
4
0
S (J mol^{-1} K^{-1})
R · ln((2·5/2)+1) = 14.9
b)
0
10
20
30
40
50
T (K)

Fig. S4

Table 1. Crystallographic data and structure refinement for Edimim[$FeCl_4$] and Edimim[$FeBr_4$] at 100K.

Molecular formula	C7 H13 Cl4 Fe N2	C7 H13 Br4 Fe N2
Formula weight	322.84	500.68
Temperature (K)	100(1)	100(2)
Wavelength (Å)	0.6193	0.71073
Crystal system	Monoclinic	Monoclinic
Space group	$P2_1/n$	$P2_1$
Unit cell dimensions	*a* = 9.6703 (1) Å α= 90°	*a* = 6.957(6) Å α= 90°
	b = 14.3513 (2) Å β= 94.261(1)°	*b* = 14.804(12) Å β= 90.728(14)°
	c = 9.5744 (1) Å γ = 90°	*c* = 7.232(6) Å γ = 90°
Volume ($Å^3$)	1325.08(3)	744.8(11)
Z	4	2
Density (calculated) (g/cm^3)	1.618	2.233
Measured 2θ range, stepsize (°)	1.104–43.092, 0.006	
Rietveld refinement details:		
Profile function	Pseudo-Voigt	
2θ range used	4.002–39.996	
Num. of reflections	2330	4861
Data points	4999	
Parameters	54	
Restraints	36	
Rwp	0.060	
$\chi_{Rietveld}$	6.130	
$\chi_{Rietveld}/\chi_{Pattern\text{-}Matching}$	1.692	
F(000)		470
Crystal size		0.10 × 0.06 × 0.06 mm^3
Theta range for data collection		2.75 to 28.38°
Index ranges		$-9 \le h \le 9$, $-19 \le k \le 18$, $-5 \le l \le 9$
Independent reflections		3158 [R(int) = 0.0581]
Completeness to theta = 28.38°		95.0 %
Max. and min. transmission		0.3963 and 0.7457
Refinement method		Full-matrix least-squares on F
Data / restraints / parameters		3158 / 72 / 146
Goodness-of-fit on F2		1.053
Final R indices [I>2sigma(I)]		R_1 = 0.0618, wR_2 = 0.1371
R indices (all data)		R_1 = 0.1135, wR_2 = 0.1563
Largest diff. peak and hole		1.306 and -1.174 $Å^{-3}$

Table 2. Most relevant interatomic distances in the crystal structure of Edimim[$FeCl_4$] at 100K.

	Edimim[$FeCl_4$] at 100K	
	Length (Å)	**Angle (º)**
H···Cl (potential hydrogen bonds)[a]		
C1'-H1A'···Cl2	3.011(10)	139.1(8)
C1'-H1B'···Cl3	2.981(6)	153.7(8)
C1''-H1A''···Cl3	3.040(11)	124.1(9)
C1''-H1C''···Cl1	3.017(11	141.2(7)
C1'''-H1B'''···Cl1	2.912(12)	148.4(5)
C1'''-H1A'''···Cl1	2.995(11)	165.3(5)
C1'''-H1C'''···Cl4	3.149(9)	120.7(9)
C2'-H2B'···Cl4	3.041(11)	116.5(8)
C2'-H2B'···Cl2	2.993(7)	122.7(4)
C4-H4···Cl1	2.846(11)	154.7(8)
C4-H4···Cl4	2.996(6)	117.3(7)
C5-H5···Cl3	2.751(10)	148.7(10)
C5-H5···Cl4	2.976(9)	117.8(10)
$[FeCl]^{-}\cdots[Dimim]^{+}$ (potential π-d interactions)		
Fe···Centroid	4.425(5)	70.8[b]
Cl4···N3	3.401(10)	
Cl4···C2	3.548(11)	
Cl2···C4	3.388(12)	
Cl2···N3	3.705(9)	
Cl4···[C4-N3]	3.414(10)	
Cl2···[C4-N3]	3.481(10)	
Cl2···Centroid	3.714(6)	101.01(16)
Cl4···Centroid	3.454(6)	100.43(16)
Cl···Cl interactions[c]		
Cl3···Cl4	4.171(5)	
Cl3···Cl1	3.936(5)	
Cl3···Cl2	4.025(5)	
Cl2···Cl1	4.192(4)	

(a) Distance smaller than the sum of vdw radii (3.05 Å for C-H···Cl)

(b) Angle between Fe–Centroid vector and the imidazolium ring plane.

(c) Sum of vdw radii for Cl···Cl is 3.7 Å.

Table 3. Most relevant interatomic distances in the crystal structure of Edimim[FeBr$_4$] at 100K.

	Edimim[FeCl$_4$] at 100K	
	Length (Å)	**Angle (º)**
H···Br (potential hydrogen bonds)[a]		
C1’’’-H1B’’’···Br4	2.725(6)	145.9(4)
C1’’’-H1B’’’···Br1	3.089(7)	119.5(6)
C5-H5···Br2	3.105(6)	156.1(11)
C4-H4···Br1	2.790(10)	161.8(7)
C1’’-H1A’’···Br4	3.076(4)	136.3(6)
C1’’-H1B···Br1	3.059(6)	144.2(9)
C1’’-H1B’’···Br3	3.133(5)	132.3(10)
[FeBr]$^-$···[Dimim]$^+$ (potential π-d interactions)		
Fe···Centroid	4.601(8)	67.4[b]
Br3···C2	3.748(6)	
Br3···N3	3.734(12)	
Br3···[N1–C2][c]	4.001(6)	
Br3···[N3–C2][c]	3.676(13)	
Br3···Centroid	4.003(10)	61.4(14)
Br4···Centroid	4.183(9)	60.2(12)
Br···Br interactions[c]		
Br3···Br4	4.095(4)	
Br4···Br1	3.985(5)	
Br3···Br2	4.053(6)	

(a) Distance smaller than the sum of vdw radii (3.15 Å for C-H···Br)

(b) Angle between Fe–Centroid vector and the imidazolium ring plane.

(c) Sum of vdw radii for Br···Br is 3.9 Å.

Table 4. Vibrational assignment (cm^{-1}) of Edimim[$FeCl_4$] at room temperature.

Experimental center / cm^{-1}	assignation
110	[$FeCl_4$]$^-$ Fe-Cl sym bend
135	[$FeCl_4$]$^-$ Fe-Cl asym bend
332	[$FeCl_4$]$^-$ Fe-Cl sym stretch
378	[$FeCl_4$]$^-$ Fe-Cl asym stretch
394	[Ethyl] CH_2-N bend, gauche conformer
579	[Ring] ip sym bend, [Ethyl] CH_2-N stretch, [Ring CH_3] CH_3-N stretch
665	[Ring] ip asym bend, [Ethyl] CH_2-N stretch, [Ring CH_3] CH_3-N stretch
711	[Ring] ip asym bend, [Ring CH_3] CH_3-N stretch
725	[Ring] HC=CH sym bend, [Ethyl] CH_2-N stretch, [Ring CH_3] CH_3-N stretch
774	[Ring] C-C sym stretch, [Ring] HC=CH sym bend, [Ring] N-C(H)-N op sym bend
801	[Ring] HC=CH sym bend, [Ring] NC(H)N op bending,
958	[Ring] ip sym bend, [Ethyl] C-C stretch
1088	[Ring] ip sym stretch, [Ethyl] CH_2-N stretch, [Ring CH_3] CH_3-N stretch
1335	
1381	[Ring] ip asym stretch, [Ethyl] C-C stretch, [Ethyl] CH_2-N stretch, [Terminal CH_3] CH_3-N stretch
1421	[Ring] ip asym stretch, [Ethyl] C-C stretch, [Ethyl] CH_2-N stretch, [Ring CH_3] CH_3-N stretch
1452	[Ring] ip asym stretch, [Ethyl] C-C stretch, [Ethyl] CH_2-N stretch, [Ring CH_3] CH_3-N stretch
2831	[Terminal CH_3] H-C-H sym stretch
2879	[Ring CH_3] H-C-H sym stretch
2932	[Ethyl] H-C-H sym stretch
2965	[Ethyl] H-C-H asym stretch
3000	[Ethyl] H-C-H asym stretch
3079	[Terminal CH_3] H-C-H asym stretch
3101	[Ring CH_3] H-C-H asym stretch
3130	[Ring N-C(H)-N] C-H stretch
3149	[Ring] HC=CH sym stretch. [Ring] ip sym stretch
3174	[Ring] HC=CH sym stretch. [Ring] ip sym stretch

Table 5. Selected geometrical parameters, bond lengths (Å) and angles (º) (experimental at 100 K) related to the possible magnetic exchange pathways for Edimim[$FeCl_4$] and Edimim[$FeBr_4$].

Magnetic exchange Pathways	Direct distance Fe-Fe/Å	Length of exchange pathway/Å	Bond/Å Fe-X	Bond/Å X-X	Bond/Å X-Fe	Angle/° Fe-X-X	Angle/° X-X-Fe	Torsion angle (τ)/º	Direction
Dimim[$FeCl_4$]									
J1 (exp.)	8.345(2)	8.578	2.211	4.171	2.196	168.90	152.65	70.38	b
J2 (exp.)	6.547(3)	8.632	2.229	4.025	2.211	143.53	82.14	168.57	a-c
J2 (exp.)	6.547(3)	8.632	2.229	4.192	2.211	146.48	78.55	165.64	a-c
J3 (exp.)	7.053(2)	8.386	2.229	3.936	2.221	108.18	138.21	125.29	a-c
Dimim[$FeBr_4$]									
J1 (exp.)	8.667(3)	8.812	2.363	4.095	2.353	166.85	161.17	84.34	b
J2 (exp.)	6.957(4)	8.691	2.355	3.985	2.351	158.02	91.19	34.15	a-c
J3 (exp.)	7.232(2)	8.776	2.372	4.053	2.351	151.28	102.28	71.72	a-c

TOC

Text for Table of Contents

We present two novel paramagnetic ionic liquids, comprised of 1-ethyl-2,3-dimethylimidazolium (Edimim) cation and tetrahaloferrate (III) (FeX_4) (X = Cl and Br) anion which display a three-dimensional magnetic ordering below 10 K. An exhaustive and systematic study of the magneto-structural correlations, involving non-bonding interactions, have been performed.

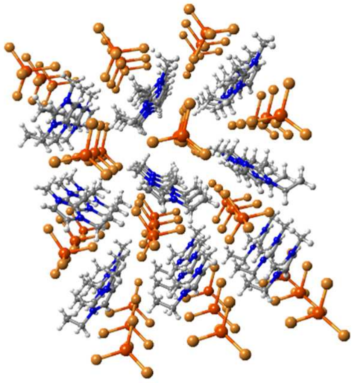

Table S1. Final refined positional coordinates from synchrotron powder X Ray diffraction pattern of Edimim[$FeCl_4$] at 100 K.

Edimim[$FeCl_4$] at 100K			
Atom	*x/a*	*y/b*	*z/c*
Fe	0.5300(2)	1.7467(2)	1.2536(4)
Cl1	0.4423(3)	1.7756(3)	1.4559(4)
Cl2	0.3625(3)	1.7637(3)	1.0826(4)
Cl3	0.7005(4)	1.8427(3)	1.2174(4)
Cl4	0.6017(4)	1.6007(2)	1.2449(4)
C1''	0.0713(11)	0.8728(7)	1.3526(4)
H1A''	0.0102	0.8231	1.2918
H1B''	0.0047	0.9155	1.4102
H1C''	0.1432	0.837	1.4238
C1'	0.3789(10)	1.1206(7)	1.1917(4)
H1A'	0.3666	1.1675	1.2769
H1B'	0.3614	1.1545	1.0923
C2'	0.5220(11)	1.0850(7)	1.1970(4)
H2A'	0.5431	1.0507	1.2955
H2B'	0.592	1.1423	1.1893
H2C'	0.5352	1.0369	1.1138
C1'''	0.2771(11)	1.0208(8)	1.4519(4)
H1A'''	0.3459	1.0794	1.4568
H1B'''	0.3303	0.9612	1.4962
H1C'''	0.1893	1.0359	1.5097
C2	0.2343(11)	1.0012(8)	1.3040(4)
N3	0.1463(9)	0.9324(7)	1.2623(4)
N1	0.2778(9)	1.0443(7)	1.1936(4)
C5	0.2095(11)	1.0065(8)	1.0721(4)
H5	0.2187	1.0261	0.9695
C4	0.1287(11)	0.9365(7)	1.1165(4)
H4	0.0632	0.8956	1.0525

Full occupancies for all atoms.
a = 9.6703(1) Å, b = 14.3513(2) Å, c = 9.5744(1) Å, $\alpha = \gamma = 90^\circ$, β = 94.261(1)°, s.g. $P2_1/n$, B_{Fe} = 2.5(2) Å^2, B_{Cl} = 2.9(1) Å^2, B_{Edimim} = 3.2(2) Å^2

Table S2. Final refined positional coordinates obtained from X Ray single crystal diffraction of Edimim[FeBr$_4$] at 100 K.

Edimim[FeBr$_4$] at 100K			
Atom	*x/a*	*y/b*	*z/c*
Fe	0.2999(3)	0.73410(14)	0.7427(3)
Br1	0.4534(2)	0.62359(11)	0.5637(3)
Br2	0.4247(2)	0.73187(12)	1.0494(2)
Br3	0.3449(2)	0.87866(10)	0.6117(2)
Br4	-0.0321(2)	0.70335(11)	0.7492(2)
C1''	1.088(3) -	1.1013(15)	0.263(3)
H1A''	0.9990	1.1233	-0.3584
H1B''	1.2036	1.0768	-0.3211
H1C''	1.1248	1.1512	-0.1806
C1'	0.948(2)	0.8567(10)	0.200(2)
H1A'	1.0849	0.8491	0.2369
H1B'	0.8960	0.7971	0.1629
C2'	0.836(3)	0.8954(19)	0.354(3)
H2A'	0.8430	0.8546	0.4606
H2B'	0.7019	0.9028	0.3146
H2C'	0.8899	0.9543	0.3885
C1'''	1.260(4)	1.003(2)	0.086(5)
H1A'''	1.2890	0.9614	0.1889
H1B'''	1.2572	1.0649	0.1320
H1C'''	1.3599	0.9970	-0.0078
C2	1.063(3)	0.9783(19)	0.000(4)
N3	0.991(4)	1.0267(17)	-0.150(4)
N1	0.930(3)	0.9221(14)	0.045(3)
C5	0.789(4)	0.9298(19)	-0.078(5)
H5	0.6857	0.8882	-0.0849
C4	0.804(4)	-1.000(2)	0.190(5)
H4	0.7119	1.0249	-0.2740

Full occupancies for all atoms.
a = 6.957(6) Å, *b* = 14.804(12) Å, *c* = 7.232(6) Å, α = γ = 90º, β = 90.728(14) º, s.g. P2_1,

Table S3. Anisotropic displacement parameters ($Å^2x10^3$) for Edimim[$FeBr_4$]. The anisotropic displacement factor exponent takes the form: $-2\pi^2[\ h^2a^{*2}U_{11} + ... + 2\ h\ k\ a^*\ b^*\ U_{12}\ ]$. U(eq) is defined as one third of the trace of the orthogonalized U_{ij} tensor.

	U_{11}	U_{22}	U_{33}	U_{23}	U_{13}	U_{12}
Br(1)	26(1)	43(1)	47(1)	0(1)	7(1)	-8(1)
Br(2)	36(1)	42(1)	33(1)	4(1)	0(1)	3(1)
Br(3)	33(1)	30(1)	39(1)	6(1)	5(1)	-6(1)
Br(4)	38(1)	38(1)	48(1)	-11(1)	6(1)	11(1)
Fe(1)	26(1)	24(1)	32(1)	2(1)	4(1)	1(1)
C(1A)	49(10)	82(16)	30(12)	12(10)	5(9)	-7(10)
C(5A)	27(7)	33(9)	25(9)	5(7)	10(6)	-2(6)
C(6A)	43(10)	130(20)	62(17)	52(15)	26(9)	44(12)
C(3A)	32(13)	49(18)	42(19)	-20(16)	-8(13)	26(12)
C(2A)	31(8)	29(9)	28(11)	1(7)	2(8)	15(8)
N(1A)	45(9)	37(8)	28(10)	-1(7)	-12(8)	16(9)
N(2A)	25(8)	20(7)	37(10)	4(7)	-4(8)	5(7)
C(4A)	33(9)	32(10)	23(11)	-1(9)	-11(8)	3(8)
C(7A)	40(9)	35(10)	23(10)	-6(8)	-7(8)	8(8)
C(1B)	49(10)	82(16)	30(12)	12(10)	5(9)	-7(10)
C(5B)	27(7)	33(9)	25(9)	5(7)	10(6)	-2(6)
C(6B)	43(10)	130(20)	62(17)	52(15)	26(9)	44(12)
C(3B)	32(13)	49(18)	42(19)	-20(16)	-8(13)	26(12)
C(2B)	31(8)	29(9)	28(11)	1(7)	2(8)	15(8)
N(1B)	45(9)	37(8)	28(10)	-1(7)	-12(8)	16(9)
N(2B)	25(8)	20(7)	37(10)	4(7)	-4(8)	5(7)
C(4B)	33(9)	32(10)	23(11)	-1(9)	-11(8)	3(8)
C(7B)	40(9)	35(10)	23(10)	-6(8)	-7(8)	8(8)